Journal of Alloys and Compounds 719 (2017) 288–295

Contents lists available at ScienceDirect

Journal of Alloys and Compounds

journal homepage: http://www.elsevier.com/locate/jalcom

Effect of glycine on one-step solution combustion synthesis of magnetite nanoparticles

Xuanli Wang [a], Mingli Qin [a, *], Fei Fang [a], Baorui Jia [a], Haoyang Wu [a], Xuanhui Qu [a], Alex A. Volinsky [b]

[a] Institute for Advanced Materials and Technology, University of Science and Technology Beijing, Beijing, 100083, China
[b] Department of Mechanical Engineering, University of South Florida, Tampa, FL 33620, USA

ARTICLE INFO

Article history:
Received 29 March 2017
Received in revised form
26 April 2017
Accepted 19 May 2017
Available online 20 May 2017

Keywords:
Solution combustion synthesis
One-step method
Fe_3O_4 nanoparticles
Glycine effects
Magnetic properties

ABSTRACT

Magnetite (Fe_3O_4) nanoparticles have been readily prepared via a one-step solution combustion synthesis (SCS) method by designing a simple airless device: a beaker with perforated rubber plug could not only separate the outside air but also release the gases generated during the combustion reaction, which could ensure an air free condition in the SCS process. The whole process did not involve any toxic or unavailable reagents, and could be finished in a few minutes by its self-generated energy derived from the redox reaction between glycine (fuel) and ferric nitrate (oxidizer). Innovatively, the combustion reaction mechanism, morphology and microstructure, phase composition and magnetic properties of SCS products in relation to the glycine have been systematically investigated. The results revealed that with the increasing molar ratio (ϕ) of glycine to ferric nitrate, the combustion mode varied from self-propagating combustion to smouldering combustion and the average grain size of SCS products increased in nanometer scale. On the contrary, the iron oxidation state of SCS products decreased with the increase of ϕ value, and the oxide phase changed from α-Fe_2O_3 to Fe_3O_4 and then to FeO sequentially. It was noteworthy that when $\phi = 0.7$, we could easily obtain pure phase Fe_3O_4 nanoparticles with the highest saturation magnetization of 89.17 emu g^{-1} and small average grain size of 57.3 nm, which would have great potential for various applications, such as magnetic drug delivery, magnetic data storage and novel ferrofluids.

1. Introduction

Magnetite (Fe_3O_4) has long been attractive material owing to its distinct physical and chemical properties [1–3]. Because of the low toxicity, high conductivity, good biocompatibility and excellent magnetic properties [4–7], nanostructured Fe_3O_4 has potential applications ranging from medical diagnostics and drug delivery to information storage and electronic devices [8], for example, magnetic resonance imaging [9], targeted drug delivery [10], magnetic recording media [11] and lithium ion batteries [12]. In recent years, multifarious methods have been developed to synthesize Fe_3O_4 nanoparticles with appropriate features (small particle size, good dispersibility, high purity and crystallinity, etc.), including high-energy ball milling [13], co-precipitation [14], micro-emulsion [15], hydrothermal synthesis [16], sol-gel method [17] and so on. However, these synthetic processes often confront the disadvantages of complicated equipment, long preparation time, multiple processing steps or environmental pollution. Besides, in the binary phase diagram of iron and oxygen, Fe_3O_4 is formed only in a very narrow stoichiometric range [18], leading to a requirement of inert-gas atmosphere, high-temperature treatment and precise controlled ratio of ingredients in the synthetic process [19–22]. Therefore, it is highly desirable to explore time- and energy-saving method for the simple and scalable preparation of Fe_3O_4 nanoparticles in an environmental-friendly way.

During the past few decades, solution combustion synthesis (SCS) has emerged as an extensive employed technique to fabricate nanomaterials, especially for nano-oxides, due to its attractive advantages of simplicity, scalability, non-pollution, time- and energy-efficiency [23–25]. It is well known that a typical SCS is substantially an exothermic redox reaction between a soluble oxidizer (e.g. metal nitrates) and an organic fuel (e.g. urea, glycine, citric acid, etc.) derived from a homogenous aqueous solution within a short

* Corresponding author.
E-mail address: qinml@mater.ustb.edu.cn (M. Qin).

http://dx.doi.org/10.1016/j.jallcom.2017.05.187
0925-8388/

time (on the order of seconds) without any additional external energy input (in a self-sustained manner), coupled with copious gas evolution (e.g. H_2O, CO_2, N_2, etc.) [26–28]. Obviously, such SCS characteristics will endow the synthesized product with some unique properties [29,30]. Firstly, the initial aqueous solution allows all the raw materials to mix on molecular level, permitting the homogenous distribution of desired composition and the precise formulation of synthesized product. Secondly, the ignition temperature needed for SCS is merely adequate triggering the combustion reaction, instead of providing the sustaining energy input (additional high-temperature calcination step) to form crystal lattice just like some traditional preparation methods, thus the high self-generated energy derived from exothermic redox reaction ensures the high purity and crystallinity of synthesized product. Thirdly, the short process duration could inhibit the growth of particle size and the formation of various gases could fragment some large agglomerates, thus leading to a fine and dispersed morphology of synthesized product. In light of the above outstanding features, a growing number of useful nano-oxides have been prepared by SCS method over the past few decades [25,27,31–33]. However, as far as we know, there are few reports on the fabrication of nanostructured Fe_3O_4 via SCS, heretofore, not to mention the direct synthesis of Fe_3O_4 nanoparticles, in a pure, crystalline state via a single SCS route.

Hence, in this work, we reported a one-step SCS method by designing a simple air exhausting device for the preparation of pure phase Fe_3O_4 nanoparticles just by tuning the molar ratio (ϕ) of fuel (glycine) to oxidizer (ferric nitrate). The whole process did not involve any toxic or unavailable reagents, and could be finished in a few minutes by its self-generated energy derived from redox reaction between glycine and ferric nitrate. In addition, the effects of ϕ value on the combustion reaction mechanism and phenomenon, morphology and microstructure, phase composition and saturation magnetization of the synthesized SCS products have been investigated systematically.

2. Experimental section

Ferric nitrate nonahydrate [$Fe(NO_3)_3 \cdot 9H_2O$] and glycine ($C_2H_5NO_2$) were supplied by Sinopharm Chemical Reagent Co., Ltd., China. Both chemicals were of analytical grade, commercially available and used as received without further purification. As shown in Fig. 1, $Fe(NO_3)_3$ and $C_2H_5NO_2$ were first dissolved in 150 mL deionized water under stirring to get a homogeneous solution. Then, the solution was poured into 1000 mL beaker with a perforated rubber plug (not only separated outside air but also released gases derived from reaction) and heated on a temperature controlled hot plate. With continuous heating, the solution evaporated and evolved into a viscous gelatinous mass. In a few minutes, a violent combustion reaction suddenly took place among or along the edge of gelatinous mass, accompanied by the liberation of voluminous gases. Noteworthily, the whole SCS process seemed to undergo a self-propagating and non-explosive combustion reaction, which took short time and resulted in the formation of fluffy nanosize powder.

Thermal analysis of the gelatinous mass was characterized in argon atmosphere from 50 °C to 600 °C at a constant heating rate of 10 °C min^{-1} by using a thermal analyzer (TG-DSC, TA Q600). Surface morphology of the SCS products was observed using field emission scanning electron microscopy (FE-SEM, Quanta FEG-450) at 30 kV. Phase analysis of the SCS products was performed on an X-ray diffractometer (XRD, Ultima IV) equipped with graphite monochromatized Cu Kα radiation as the X-ray source. The average grain size of SCS products was calculated according to the Debye-Scherrer formula [34], $D = K\lambda/\beta\cos\theta$, where D was the average grain size, K was a constant related to the shape of grain, λ was the wavelength of employed radiation, β was the peak width (full width at half maximum, FWHM) in radians, and θ was the Bragg diffraction angle. The surface composition of SCS products was analyzed by X-ray photoelectron spectroscopy (XPS, Thermo EscaLab 250Xi) at a background pressure of about 10^{-9} Torr using Al Kα X-rays as the excitation source (1486.6 eV). Magnetic measurements were carried out using the physical properties measurement system (PPMS) in a vibrating sample magnetometer (VSM, BKT-4500) with a magnetic field varied in the ±6000 Oe range.

3. Results and discussion

In SCS process, the fuel to oxidizer molar ratio has been previously shown to alter the thermal behavior, oxidation state, morphology and properties of products [35,36]. Thus, in this work, the molar ratio of glycine (variate) to ferric nitrate (constant), denoted as $\phi = (n_{Gly} - n_{Fe})/n_{Fe}$, was taken to be 0.5 (fuel-lean condition), 0.7 (stoichiometric equilibrium), 1.2 and 1.6 (fuel-rich condition), according to the propellant chemistry theory proposed by Jain et al., [37] as described in Eq. (1).

$$54Fe(NO_3)_3 + 92C_2H_5NO_2 = 18Fe_3O_4 + 184CO_2 + 230H_2O + 127N_2 \quad (1)$$

In order to explore the combustion reaction mechanism in SCS process, the gelatinous mass obtained from different ϕ reaction systems were heated from 50 °C to 600 °C in argon atmosphere at a heating rate of 10 °C min^{-1} by using thermogravimetry (TG)-differential scanning calorimetry (DSC). The resulting TG-DSC curves are presented in Fig. 2. According to the shape of curves, the whole reaction procedure can be clearly divided into three temperature stages. In the first stage (100–150 °C), Fig. 2 (a, b) show a weak and wide endothermic peak accompanied by a major weight loss of ~30%, while Fig. 2 (c, d) display a relatively distinct and narrow endothermic peak at around 130 °C coupled with a minor weight loss of ~10%. The observed ~10% weight loss in $\phi = 1.2$ and 1.6 reaction systems can be ascribed to the vaporization of residual water and desorption of chemically absorbed water in the gelatinous mass. By comparison, the observed ~30% weight loss in $\phi = 0.5$ and 0.7 reaction systems can be attributed to the superposition of the removal of various types of water and the partial decomposition of excessive ferric nitrate in fuel-lean condition. In light of the corresponding weak and wide endothermic characteristic on DSC curves (Fig. 2 a and b), it is a reasonable inference that the decomposition of ferric nitrate is a slow and moderate process. In the second stage (150–200 °C), all the reaction systems undergo an abrupt weight loss on the TG curves and a drastic exothermic peak at ~160 °C is presented on the DSC curves, which are in relation to the thermally induced redox reaction between ferric nitrate and glycine. As depicted in Fig. 2(a–d), it is apparent that with the increase of ϕ value, the position of exothermic peak seems immobile while its shape changes from sharp to a little wide, especially in $\phi = 1.6$ reaction system, the exothermic peak become bimodal, which may be attributed to the synergy effects of the combustion reaction between ferric nitrate and glycine and the reduction reaction of ferric ions. Actually, glycine can not only serve as a fuel during the combustion reaction, but also act as a reducing agent being oxidized by nitrate ions, at the same time, the ferric ions in ferric nitrate will be reduced by amino group in glycine. It is well known that the more reducing agent exists in reaction system, the stronger reduction ability it owns. Thus, in this ferric nitrate-glycine

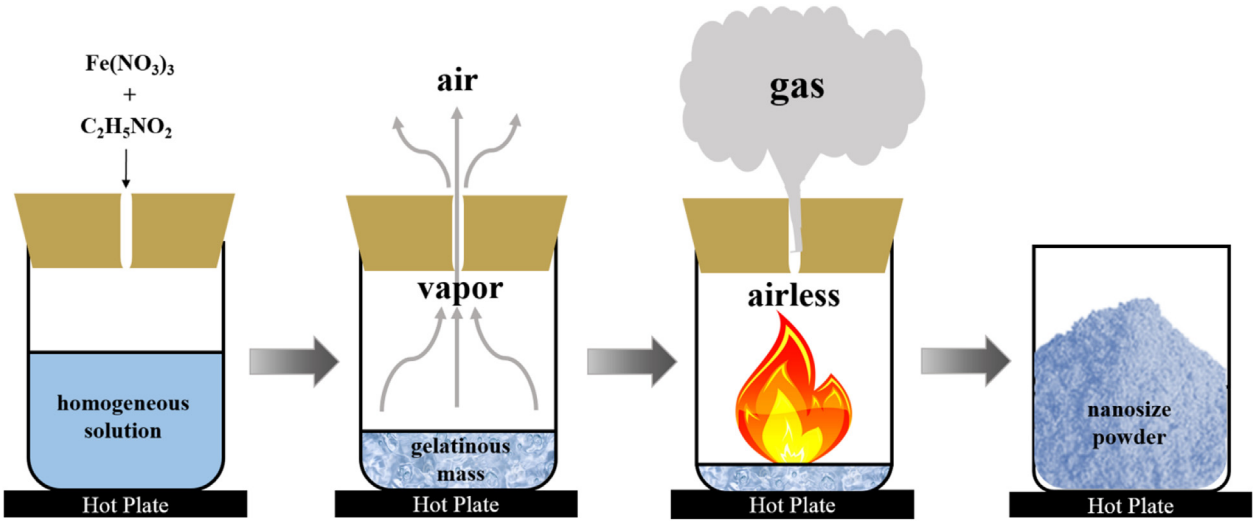

Fig. 1. Schematic illustration of SCS process for the ferric nitrate-glycine reaction system.

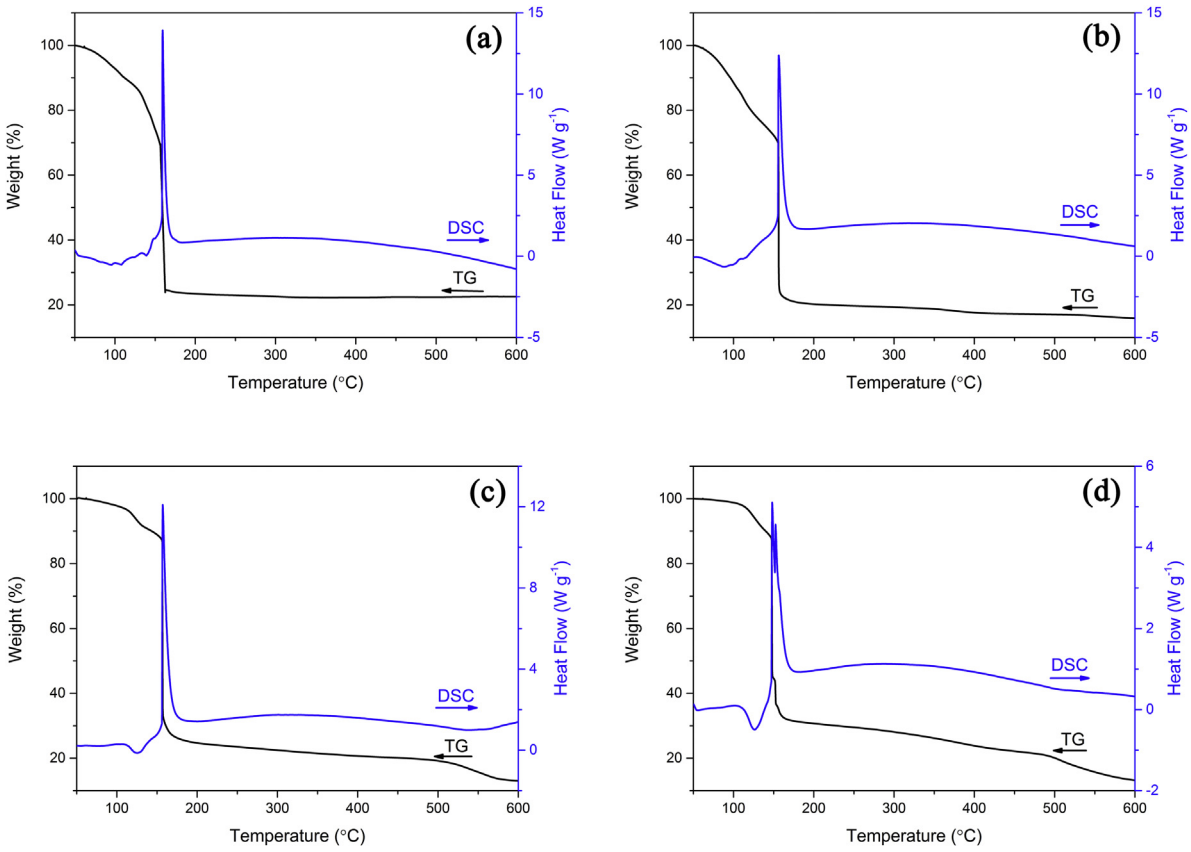

Fig. 2. TG-DSC curves of the gelatinous mass obtained from different ϕ reaction systems:(a) ϕ = 0.5; (b) ϕ = 0.7; (c) ϕ = 1.2; (d) ϕ = 1.6.

reaction system, with the increase of ϕ value, the reducing degree of ferric ions (Fe^{3+}) deepens and they will be successfully reduced into ferrous ions (Fe^{2+}) in the lean oxygen environment. On the basis of above analysis, we can deduce that ϕ = 0.5 reaction system is inclined to follow Eq. (2) and obtain some Fe_2O_3 phase, ϕ = 0.7 reaction system tends to follow Eq. (1) and form pure Fe_3O_4 phase, while the fuel-rich reaction systems (ϕ = 1.2 and 1.6) are apt to comply with Eq. (3) and get some FeO phase except for the Fe_3O_4 phase.

$$6Fe(NO_3)_3 + 10C_2H_5NO_2 = 3Fe_2O_3 + 20CO_2 + 25H_2O + 14N_2 \quad (2)$$

$$18Fe(NO_3)_3 + 32C_2H_5NO_2 = 18FeO + 64CO_2 + 80H_2O + 43N_2 \quad (3)$$

Finally, in the third stage (above 200 °C), the weight of samples in ϕ = 0.5 and 0.7 reaction systems keeps almost constant, implying

the end of combustion reaction. However, when the temperature surpasses 500 °C, another small endothermic peak appears in $\phi = 1.2$ and 1.6 reaction system. This may be ascribed to the carbonization process, which is generated by the decomposition of excessive glycine in fuel-rich reaction system.

The visual reaction processes and original appearance photographs of SCS products obtained from different ϕ reaction systems are shown in Figs. 3 and 4, respectively. From Fig. 3, it can be clearly observed that all the reaction processes involve a transition from solution to gelatinous mass and then occur a combustion reaction coupled with the liberation of voluminous gases. It is evident that the whole reaction process takes place in the beaker with a perforated rubber plug, which can ensure the lean oxygen environment for these two reasons: first, in the preheating process, the evaporation of various types of water will take away the air inside beaker, namely, the water vapor pressure can force the residual oxygen spilling from the small hole in rubber plug, ensure that the subsequent combustion reaction can happen under a nearly oxygen-free condition; second, in the combustion reaction process, the liberation of voluminous gases will prevent the outside air from slipping into the beaker, ensure that the combustion reaction carries out under an oxygen-free condition. Simultaneously, when comparing the combustion reaction phenomena of different ϕ reaction systems, we can find that the combustion mode varies from self-propagating combustion to smouldering combustion with the increase of ϕ value. As shown in Fig. 3(a), $\phi = 0.5$ reaction system exhibits a self-propagating combustion mode, i.e. the flame starts at a certain point of gelatinous mass and then spreads to the whole beaker, accompanied by the release of voluminous gases. It is obvious that the released gases are reddish brown, indicating that there is NO_x gaseous byproduct generated during the combustion reaction. It is worth noting that the self-propagating combustion reaction only lasts for 10 s or so, forming some spongy dark red powders in the beaker, as shown in Fig. 4(a). Considering the color of obtained powders and TG-DSC analysis result (Fig. 2a), it can be inferred that the SCS product of $\phi = 0.5$ reaction system contains both crystalline Fe_2O_3 and Fe_3O_4 phases. By comparison, $\phi = 0.7$

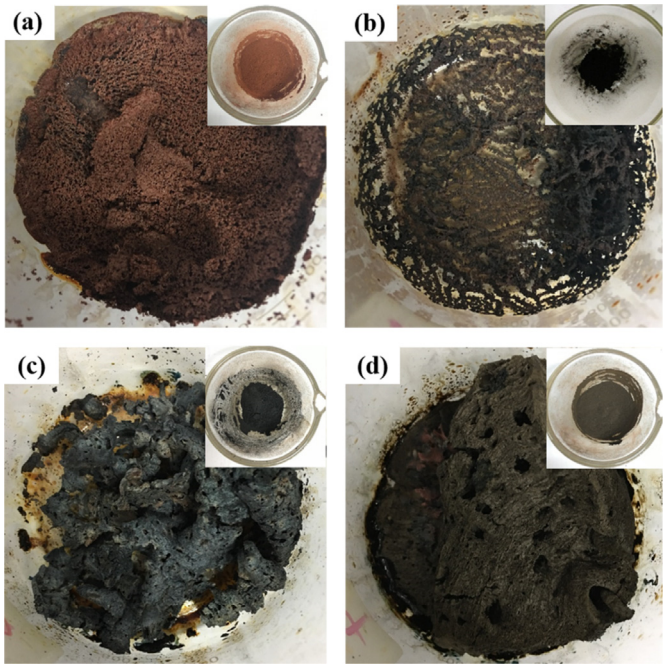

Fig. 4. Photographic images of SCS products obtained from different ϕ reaction systems. (the up-right inset shows the corresponding image of grinding product): (a) $\phi = 0.5$; (b) $\phi = 0.7$; (c) $\phi = 1.2$; (d) $\phi = 1.6$.

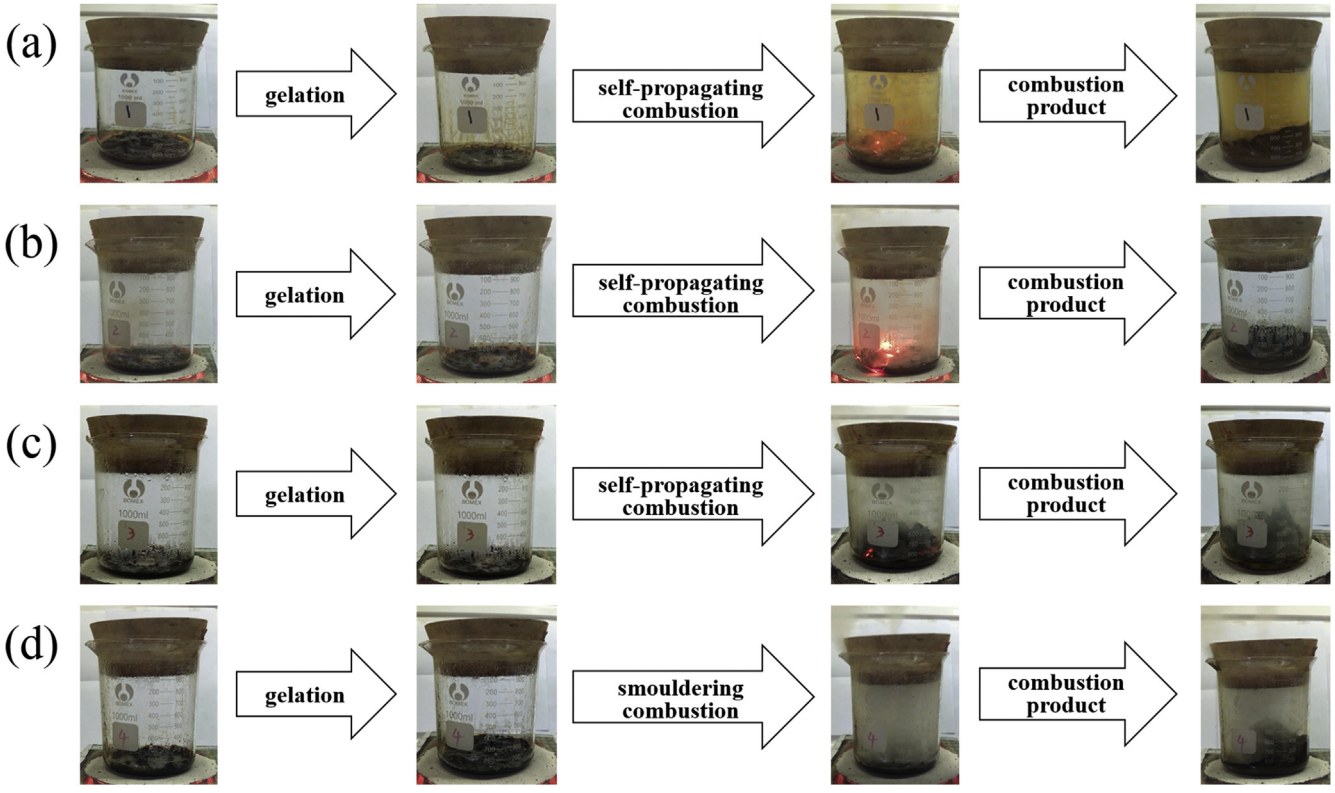

Fig. 3. Reaction processes of different ϕ reaction systems: (a) $\phi = 0.5$; (b) $\phi = 0.7$; (c) $\phi = 1.2$; (d) $\phi = 1.6$.

and 1.2 reaction systems (Fig. 3b and c) also exhibit a self-propagating combustion mode as depicted in $\phi = 0.5$ reaction system. However, the released gases in these two reaction systems are colorless and the flame in Fig. 3(b) appears brighter than that in Fig. 3(c). When comparing the morphology of SCS products, it can be noticed from Fig. 4(b and c) that $\phi = 0.7$ reaction system yields some loose dendritic black powders while $\phi = 1.2$ reaction system produces some fluffy foamy black powders in the beaker. In contrast, as shown in Fig. 3(d), $\phi = 1.6$ reaction system exhibits a smouldering combustion mode, i.e. the gelatinous mass swells continuously with no bright flame and large numbers of white gases liberate successively. After about 20 s, the reaction finishes and some stalactite shaped black grey powders appear in the beaker (Fig. 4d). This phenomenon may be attributed to the carbonization of excessive glycine in fuel-rich reaction system, which has been already proposed by TG-DSC analysis in Fig. 2(d). Furthermore, considering the black grey color of obtained powders (Fig. 4d), it is reasonable to deduce that the SCS product of $\phi = 1.6$ reaction system contains amorphous carbon and some mixed FeO_x ($1 < x < 1.5$) phases.

To acquire more information about morphology of SCS products obtained from different ϕ reaction systems, they are investigated by FE-SEM, as shown in Fig. 5. It can be clearly observed that all the SCS products exhibit an assorted mass of agglomerated particles with a wide distribution, meanwhile, some irregular sized and shaped voids exist among the agglomerates, which is due to the drastic release of voluminous gases generated from the violent combustion reaction. With the increase of ϕ value, the agglomerates become denser, larger and more durable. It is obvious that the agglomerates in fuel-lean product ($\phi = 0.5$) involve thick slices and small particles in the microscale range (Fig. 5a), similarly, the agglomerates in stoichiometric equilibrium product ($\phi = 0.7$) mainly consist of blocky particles with a narrow size distribution (Fig. 5b). In contrast to this, the agglomerates in fuel-rich products ($\phi = 1.2$ and 1.6) show a complex microstructure in the bulk form, which are composed of regular quadrate nanoparticles smaller than 500 nm in size (Fig. 5c and d). Those distinctive morphologies of SCS products indicate that the particles are inclined to aggregate owing to the influence of nano effects, meanwhile, the dispersant effect of released gases could disjoin the agglomerates and the high energy generated during the combustion reaction process could accelerate the crystal growth [38,39].

Fig. 6(a) shows XRD patterns of the SCS products with different ϕ. It is clear that the $\phi = 0.5$ product is a mixture of α-Fe_2O_3 (JCPDS card No.89-0599) and Fe_3O_4 (JCPDS card No. 89-0691) according to the diffraction peak positions [40], which is in excellent agreement with the dark red color (Fig. 4a) and TG-DSC analysis (Fig. 2a) as mentioned above. In the pattern of $\phi = 0.7$ product, the crystalline Fe_3O_4 phase with sharp diffraction peaks can be detected and no additional peaks have been observed, demonstrating the purity of Fe_3O_4. This is well consistent with the black color of $\phi = 0.7$ product as shown in Fig. 4(b) and fits in with the tendency of Eq. (1) as analyzed by TG-DSC results (Fig. 2b). In contrast, except for the Fe_3O_4 phase, three tiny new diffraction peaks centered at about $2\theta = 41.9°$, 60.8° and 76.6°appear in the XRD pattern of $\phi = 1.2$ product and correspond to the predominant reflection (200), (220) and (222) of FeO (JCPDS card No.75-1550) [40], indicating the reduction of Fe_3O_4, which is in accord with the inference that fuel-rich reaction system tends to comply with Eq. (3) as evidenced in Fig. 2(c). On the basis of above analysis, the change of phases in these SCS products confirms that in the combustion process, glycine acts not only as a fuel, but also as a reducing agent, resulting in the rapid reduction of Fe^{3+} to Fe^{2+}. Thus, with the increase of ϕ value, the phase of SCS product tends to change from α-Fe_2O_3 to

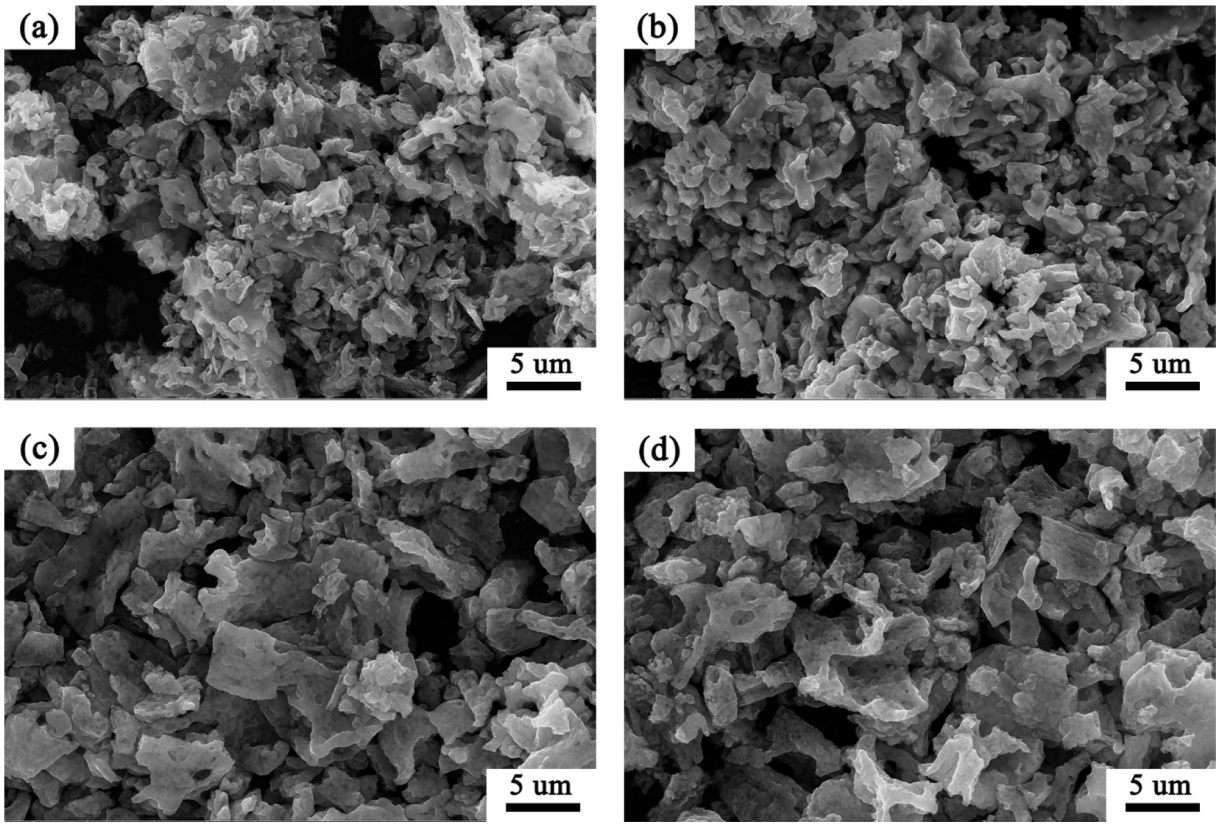

Fig. 5. FE-SEM images of SCS products obtained from different ϕ reaction systems: (a) $\phi = 0.5$; (b) $\phi = 0.7$; (c) $\phi = 1.2$; (d) $\phi = 1.6$.

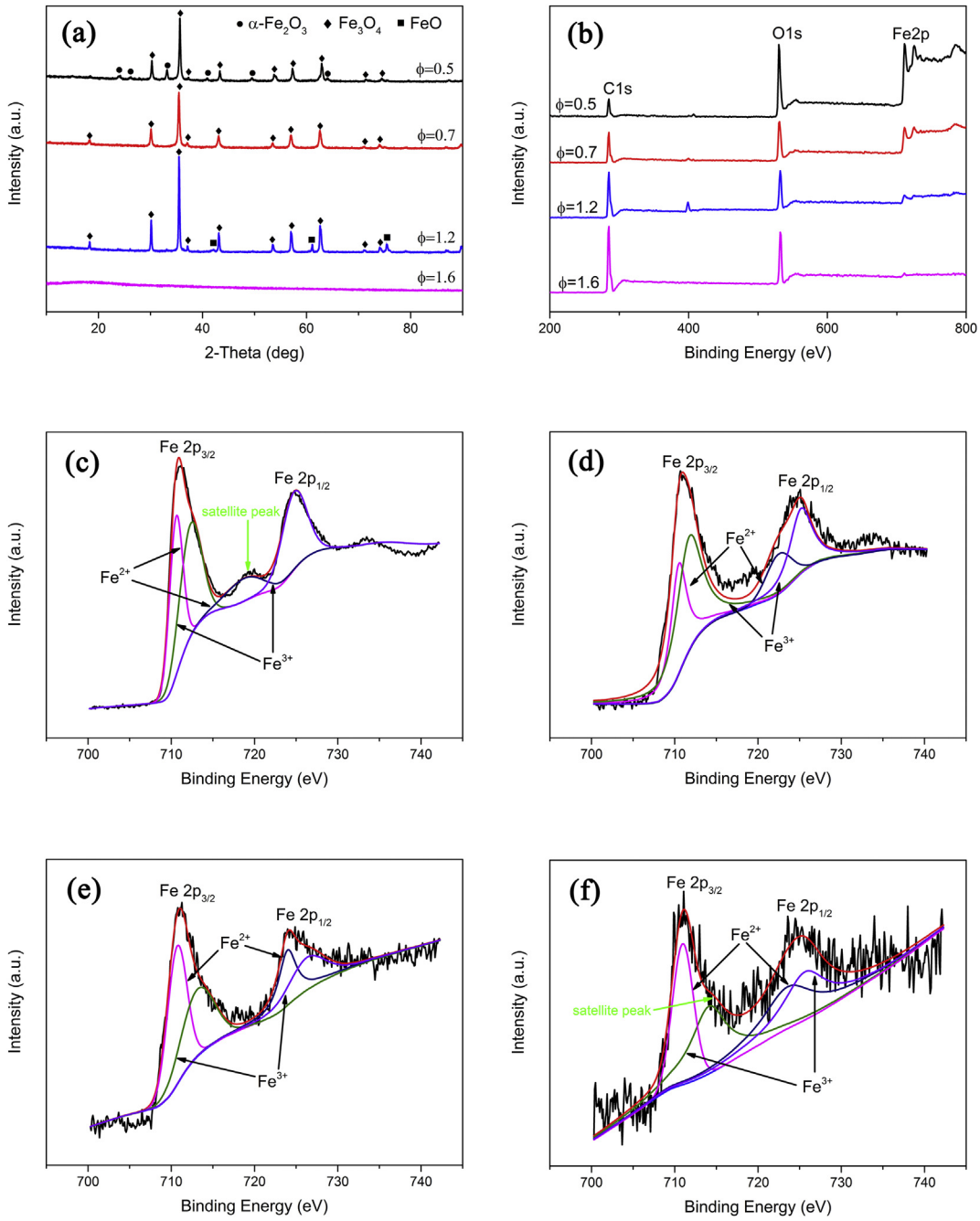

Fig. 6. (a) XRD patterns, (b) full range XPS spectra and (c–f) Fe2p high-resolution XPS spectra of SCS products obtained from different ϕ reaction systems: (c) ϕ = 0.5; (d) ϕ = 0.7; (e) ϕ = 1.2; (f) ϕ = 1.6.

Fe_3O_4 and then to FeO sequentially. In addition, the average grain size of these SCS products deduced from Debye-Scherrer formula is about 39.1 nm, 57.3 nm and 87.4 nm, respectively. It is evident that these SCS products are composed of nanocrystals and the average grain size enlarges with the increase of ϕ value. However, when the value of ϕ increases to 1.6, there is no obvious Bragg diffraction peak that can be detected in the corresponding XRD pattern, implying the amorphous structure of ϕ = 1.6 product. This may be ascribed to the carbonization of excessive glycine in ϕ = 1.6 reaction system, which could form some amorphous carbon floating on the surface of product, resulting in the weakening of iron oxide phases.

In order to further verify the crystal phase of iron oxide in SCS products with different ϕ, X-ray photoelectron spectra of these products are shown in Fig. 6(b–f). On the one hand, the survey XPS spectra in Fig. 6(b) represent the full range of binding energy from 200 to 800 eV, demonstrating that the main chemical components in all the SCS products are C (1s), O (1s) and Fe (2p). With the increase of ϕ value, the characteristic peak of C1s enhances, while the intensities of O1s and Fe2p peaks become lower and lower. This phenomenon demonstrates that the amorphous carbon obtained from the carbonization of excessive glycine in fuel-rich reaction system floats on the surface of product, leading to the weakening of iron oxides phase, which is in conformity to the above XRD analysis. On the other hand, the Fe2p high-resolution XPS spectra of all the SCS products (Fig. 6c–f) can be resolved into two binding energy

peaks positioned at 710.4 and 723.8 eV, which are assigned to the Fe $2p_{3/2}$ and Fe $2p_{1/2}$, respectively [12]. Moreover, the peaks of Fe $2p_{3/2}$ and Fe $2p_{1/2}$ could be further deconvoluted into four component peaks with binding energies of about 709.2 eV (722.4 eV) corresponding to the Fe $2p_{3/2}$ (Fe $2p_{1/2}$) for Fe^{2+} and 711.1 eV (724.5 eV) corresponding to the Fe $2p_{3/2}$ (Fe $2p_{1/2}$) for Fe^{3+}, respectively, revealing the formation of mixed valence ions of Fe^{2+} and Fe^{3+} in these products [41]. It is noteworthy that the Fe $2p_{3/2}$ peak in Fig. 6(c) is linked with a charge transfer satellite peak located at about 8 eV higher than the main peak, which is a major characteristic of α-Fe_2O_3 [42], indicating that $\phi = 0.5$ product contains both α-Fe_2O_3 and Fe_3O_4 phases as confirmed by the above XRD analysis. Similarly, it can be noticed from Fig. 6(f) that there seems to be another charge transfer satellite peak at about 715 eV alongside the Fe $2p_{3/2}$ peak, which is a typical characteristic of FeO [43], further demonstrating that the iron oxide phases in $\phi = 1.6$ product are Fe_3O_4 and FeO. In addition, since Fe_3O_4 could also be expressed as $FeO{\cdot}Fe_2O_3$, the atomic ratio of Fe^{2+}:Fe^{3+} should be equal to 1:2 or 0.33:0.67. In Fig. 6(d and e), the relative areas of deconvoluted peaks at around 709.2 eV and 711.1 eV (assigned to Fe^{2+} and Fe^{3+} in Fe $2p_{2/3}$ peak) for $\phi = 0.7$ and 1.2 products are calculated to be ~0.5 and ~0.8, respectively [3,44], indicating the pure Fe_3O_4 phase in $\phi = 0.7$ product and mixed oxide phases of Fe_3O_4 and FeO in $\phi = 1.2$ product, which are in excellent accordance with the above XRD analysis in Fig. 6(a).

The magnetic properties of SCS products with different ϕ are characterized by VSM and the corresponding magnetic hysteresis loops are presented in Fig. 7. Obviously, all the SCS products present typical ferromagnetic type curves and $\phi = 0.7$ product owns the highest saturation magnetization of 89.17 emu g^{-1} due to its high Fe_3O_4 purity, as already proved by the above XRD and XPS analysis. However, this saturation magnetization value still lower than that of bulk Fe_3O_4 (92 emu g^{-1}), which may be ascribed to the distinct surface effects in these Fe_3O_4 nanoparticles. To be specific, the disordered spins existed in the surface of nanoparticles, due to the nano effects, would hinder the core spins inside nanoparticles from aligning along the direction of magnetic field, thus the saturation magnetization of nanoparticles will decrease inevitably [45]. Moreover, it is well known that the saturation magnetization also relies upon the crystallinity and chemical composition of magnetic nanoparticles [27]. Accordingly, $\phi = 0.5$ and 1.2 products possess a relatively low saturation magnetization (72.79 emu g^{-1} and 84.75 emu g^{-1} respectively) as compared to $\phi = 0.7$ product. The saturation magnetization values decrease as a result of the existence of weak magnetic α-Fe_2O_3 phase in $\phi = 0.5$ product and the reduction

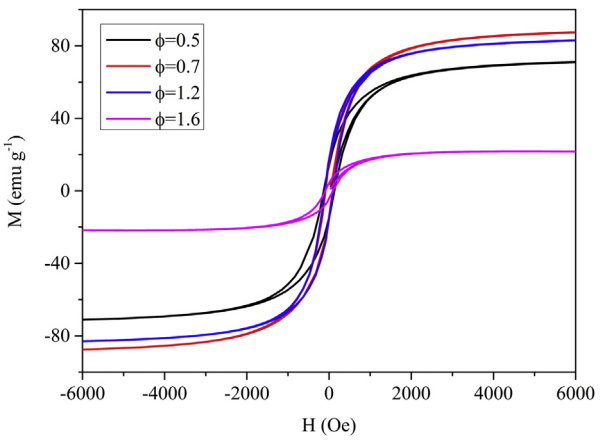

Fig. 7. Magnetic hysteresis loops of SCS products obtained from different ϕ reaction systems.

of a small portion of magnetic Fe_3O_4 phase in $\phi = 1.2$ product. In addition, as the ϕ value increases to 1.6, the saturation magnetization of product steeply decreases to 21.82 emu g^{-1} due to the amorphous carbon composition and the low crystallinity of mixed iron oxide phases, as already demonstrated by the above XRD and XPS analysis. It is distinct that such variation tendency of saturation magnetization with the increase of ϕ value conforms to the above dependence of magnetic properties upon the particle size, crystallinity and composition. Thus, the significant contribution of SCS method herein is to synthesize the pure Fe_3O_4 nanoparticles with small particle size, high crystallinity and good magnetic performance, which would have great potential for various applications, such as magnetic drug delivery, magnetic data storage and novel ferrofluids.

4. Conclusions

In conclusion, synthesis of Fe_3O_4 nanoparticles was carried out via a facile solution combustion synthesis (SCS) process by using ferric nitrate as the oxidizer and glycine as the fuel in a single route. It was concluded that the molar ratio (ϕ) of glycine to ferric nitrate has a great influence on the combustion reaction mechanism, phase composition, morphology and magnetic properties of SCS products. With the increase of ϕ value, the combustion mode varied from self-propagating combustion to smouldering combustion and the oxide phase of SCS products changed from α-Fe_2O_3 to Fe_3O_4 to FeO sequentially. It was worth noting that when $\phi = 0.7$, we could easily obtain pure phase Fe_3O_4 nanoparticles with the highest saturation magnetization of 89.17 emu g^{-1} and small average grain size of 57.3 nm, which were not only beneficial to industrial production but also promising for technological application.

Acknowledgements

This work was financially supported by the National Natural Science Foundation Program of China (51574031, 51574030 and 51574029), the Natural Science Foundation Program of Beijing (2162027), the National 863 Program (2013AA031101), the China Postdoctoral Science Foundation (2016M591073) and the Fundamental Research Funds for the Central Universities (FRF-TP-15-062A1).

References

[1] X. Zhang, D. Han, Z. Hua, S. Yang, Porous Fe_3O_4 and gamma-Fe_2O_3 foams synthesized in air by sol-gel autocombustion, J. Alloy. Compd. 684 (2016) 120–124.
[2] E. Karaca, M. Şatır, S. Kazan, M. Açıkgöz, E. Öztürk, G. Gürdağ, D. Ulutaş, Synthesis, characterization and magnetic properties of Fe_3O_4 doped chitosan polymer, J. Magn. Magn. Mater 373 (2015) 53–59.
[3] R. Ianoş, A. Tăculescu, C. Păcurariu, I. Lazău, Solution combustion synthesis and characterization of magnetite, Fe_3O_4, nanopowders, J. Am. Ceram. Soc. 95 (2012) 2236–2240.
[4] H. He, C. Gao, Superparamagnetic, conductive, and processable multifunctional graphene nanosheets coated with high-density Fe_3O_4 nanoparticles, Acs. Appl. Mater. Inter 2 (2010) 3201–3210.
[5] D.D. Suppiah, S.B. Abd Hamid, One step facile synthesis of ferromagnetic magnetite nanoparticles, J. Magn. Magn. Mater 414 (2016) 204–208.
[6] J. Rodríguez-Chueca, A. Mediano, N. Pueyo, I. García-Suescun, R. Mosteo, M.P. Ormad, Degradation of chloroform by Fenton-like treatment induced by electromagnetic fields: a case of study, Chem. Eng. Sci. 156 (2016) 89–96.
[7] P. Jayakrishnan, M.T. Ramesan, Studies on the effect of magnetite nanoparticles on magnetic, mechanical, thermal, temperature dependent electrical resistivity and DC conductivity modeling of poly (vinyl alcohol-co-acrylic acid)/Fe_3O_4 nanocomposites, Mater. Chem. Phys. 186 (2017) 513–522.
[8] Y. Zhu, W. Zhao, A. Chen, J. Shi, A simple one-pot self-assembly route to nanoporous and monodispersed Fe_3O_4 particles with oriented attachment structure and magnetic property, J. Phys. Chem. C 111 (2007) 5281–5285.
[9] L. Wu, M. Wu, X. Lin, X.L. Zhang, X. Liu, J. Liu, Magnetite nanocluster and paclitaxel loaded charge-switchable nanohybrids for MR Imaging and chemotherapy, J. Mater. Chem. B 5 (2017) 849–857.

[10] M. Salem, Y. Xia, A. Allan, S. Rohani, E.R. Gillies, Curcumin-loaded, folic acid-functionalized magnetite particles for targeted drug delivery, Rsc. Adv. 5 (2015) 37521–37532.
[11] U. Khan, N. Adeela, M. Irfan, H. Ali, X.F. Han, Temperature mediated morphological and magnetic phase transitions of iron/iron oxide core/shell nanostructures, J. Alloy. Compd. 696 (2017) 362–368.
[12] Y. Jiao, H. Zhang, T. Dong, P. Shen, Y. Cai, H. Zhang, S. Zhang, Improved electrochemical performance in nanoengineered pomegranate-shaped Fe_3O_4/RGO nanohybrids anode material, J. Mater. Sci. 52 (2017) 3233–3243.
[13] J.F. de Carvalho, S.N. de Medeiros, M.A. Morales, A.L. Dantas, A.S. Carriço, Synthesis of magnetite nanoparticles by high energy ball milling, Appl. Surf. Sci. 275 (2013) 84–87.
[14] F. Yazdani, M. Seddigh, Magnetite nanoparticles synthesized by co-precipitation method: the effects of various iron anions on specifications, Mater. Chem. Phys. 184 (2016) 318–323.
[15] Z.H. Zhou, J. Wang, X. Liu, H. Chan, Synthesis of Fe_3O_4 nanoparticles from emulsions, J. Mater. Chem. 11 (2001) 1704–1709.
[16] M. Chen, L.L. Shao, J.J. Li, W.J. Pei, M.K. Chen, X.H. Xie, One-step hydrothermal synthesis of hydrophilic Fe_3O_4/carbon composites and their application in removing toxic chemicals, Rsc. Adv. 6 (2016) 35228–35238.
[17] Z.Z. Xu, C.C. Wang, W.L. Yang, S.K. Fu, Synthesis of superparamagnetic Fe_3O_4/SiO_2 composite particles via sol-gel process based on inverse miniemulsion, J. Mater. Sci. 40 (2005) 4667–4669.
[18] L.S. Darken, R.W. Gurry, The system iron-oxygen. II. equilibrium and thermodynamics of liquid oxide and other phases, J. Am. Chem. Soc. 68 (1946) 798–816.
[19] G.P. Nagabhushana, G.T. Chandrappa, Facile solution combustion synthesis of monoclinic VO_2: a unique and versatile approach, J. Mater. Chem. A 1 (2013) 11539–11542.
[20] H. Li, Y. Li, Y. Zhang, C. Zhang, Facile synthesis of carbon-coated Fe_3O_4 core-shell nanoparticles as anode materials for lithium-ion batteries, J. Nanopart. Res. 17 (2015) 1–9.
[21] Y.C. Dong, R.G. Ma, M.J. Hu, H. Cheng, C.K. Tsang, Q.D. Yang, Y.Y. Li, J.A. Zapien, Scalable synthesis of Fe_3O_4 nanoparticles anchored on graphene as a high-performance anode for lithium ion batteries, J. Solid. State. Chem. 201 (2013) 330–337.
[22] O. Khani, M.Z. Shoushtari, M. Jazirehpour, M.H. Shams, Effect of carbon shell thickness on the microwave absorption of magnetite-carbon core-shell nanoparticles, Ceram. Int. 42 (2016) 14548–14556.
[23] W. Wen, J.M. Wu, Nanomaterials via solution combustion synthesis: a step nearer to controllability, Rsc. Adv. 4 (2014) 58090–58100.
[24] H.Q. Jiang, H. Endo, H. Natori, M. Nagai, K. Kobayashi, Fabrication and photoactivities of spherical-shaped $BiVO_4$ photocatalysts through solution combustion synthesis method, J. Eur. Ceram. Soc. 28 (2008) 2955–2962.
[25] A. Varma, A.S. Mukasyan, A.S. Rogachev, K.V. Manukyan, Solution combustion synthesis of nanoscale materials, Chem. Rev. 116 (2016) 14493–14586.
[26] S.L. González-Cortés, F.E. Imbert, Fundamentals, properties and applications of solid catalysts prepared by solution combustion synthesis (SCS), Cheminform 452 (2013) 117–131.
[27] M. Huang, M. Qin, D. Zhang, Y. Wang, Q. Wan, Q. He, B. Jia, X. Qu, Facile synthesis of sheet-like Fe/C nanocomposites by a combustion-based method, J. Alloy. Compd. 695 (2016) 1870–1877.
[28] K.V. Manukyan, A. Cross, S. Roslyakov, S. Rouvimov, A.S. Rogachev, E.E. Wolf, A.S. Mukasyan, Solution combustion synthesis of nano-crystalline metallic materials: mechanistic studies, J. Phys. Chem. C 117 (2013) 24417–24427.
[29] K. Rajeshwar, N.R.D. Tacconi, Solution combustion synthesis of oxide semiconductors for solar energy conversion and environmental remediation, Chem. Soc. Rev. 38 (2009) 1984–1998.
[30] F.T. Li, J. Ran, M. Jaroniec, S.Z. Qiao, Solution combustion synthesis of metal oxide nanomaterials for energy storage and conversion, Nanoscale 7 (2015) 17590–17610.
[31] V.D. Zhuravlev, V.G. Bamburov, A.R. Beketov, L.A. Perelyaeva, I.V. Baklanova, O.V. Sivtsova, V.G. Vasil'Ev, E.V. Vladimirova, V.G. Shevchenko, I.G. Grigorov, Solution combustion synthesis of α-Al_2O_3 using urea, Ceram. Int. 39 (2013) 1379–1384.
[32] M.D. Lima, R. Bonadimann, M.J.D. Andrade, J.C. Toniolo, C.P. Bergmann, Nanocrystalline Cr_2O_3 and amorphous CrO_3 produced by solution combustion synthesis, J. Eur. Ceram. Soc. 26 (2006) 1213–1220.
[33] V.R. Orante-Barrón, F.M. Escobar-Ochoa, C. Cruz-Vázquez, R. Bernal, Thermoluminescence of novel zinc oxide nanophosphors obtained by glycine-based solution combustion synthesis, J. Nanomater 2015 (2015) 1–5.
[34] U. Holzwarth, N. Gibson, The scherrer equation versus the 'Debye-Scherrer equation, Nat. Nanotechnol 6 (2011) 534.
[35] S.T. Aruna, N.S. Kini, K.S. Rajam, Solution combustion synthesis of CeO_2-$CeAlO_3$ nano-composites by mixture-of-fuels approach, Mater. Res. Bull. 44 (2009) 728–733.
[36] K. Tahmasebi, M.H. Paydar, The effect of starch addition on solution combustion synthesis of Al_2O_3-ZrO_2 nanocomposite powder using urea as fuel, Mater. Chem. Phys. 109 (2008) 156–163.
[37] S.R. Jain, K.C. Adiga, V.R.P. Verneker, A new approach to thermochemical calculations of condensed fuel-oxidizer mixtures, Combust. Flame 40 (1981) 71–79.
[38] J. Toniolo, A.S. Takimi, M.J. Andrade, R. Bonadiman, C.P. Bergmann, Synthesis by the solution combustion process and magnetic properties of iron oxide (Fe_3O_4 and α-Fe_2O_3) particles, J. Mater. Sci. 42 (2007) 4785–4791.
[39] M.A. Rodríguez, C.L. Aguilar, M.A. Aghayan, Solution combustion synthesis and sintering behavior of $CaAl_2O_4$, Ceram. Int. 38 (2012) 395–399.
[40] J. Han, X. Zong, Z. Wang, C. Li, A hematite photoanode with gradient structure shows an unprecedentedly low onset potential for photoelectrochemical water oxidation, Phys. Chem. Chem. Phys. 16 (2014) 23544–23548.
[41] R. Prakash, R.J. Choudhary, L.S.S. Chandra, N. Lakshmi, D.M. Phase, Electrical and magnetic transport properties of Fe_3O_4 thin films on GaAs (100) substrate, J. Phys. Condens. Matter 19 (2007) 486212.
[42] T. Yamashita, P. Hayes, Analysis of XPS spectra of Fe^{2+} and Fe^{3+} ions in oxide materials, Appl. Surf. Sci. 254 (2008) 2441–2449.
[43] P.C.J. Graat, M.A.J. Somers, Simultaneous determination of composition and thickness of thin iron-oxide films from XPS Fe 2p spectra, Appl. Surf. Sci. 100–101 (1996) 36–40.
[44] J. Gao, X. Ran, C. Shi, H. Cheng, T. Cheng, Y. Su, One-step solvothermal synthesis of highly water-soluble, negatively charged superparamagnetic Fe_3O_4 colloidal nanocrystal clusters, Nanoscale 5 (2013) 7026–7033.
[45] S.A. Kulkarni, P.S. Sawadh, P.K. Palei, K.K. Kokate, Effect of synthesis route on the structural, optical and magnetic properties of Fe_3O_4 nanoparticles, Ceram. Int. 40 (2013) 1945–1949.